THE JOURNAL OF PHYSICAL CHEMISTRY LETTERS
A JOURNAL OF THE AMERICAN CHEMICAL SOCIETY

pubs.acs.org/JPCL

Letter

Machine-Learning Accelerated First-Principles Accurate Modeling of the Solid−Liquid Phase Transition in MgO under Mantle Conditions

Pandu Wisesa,[†] Christopher M. Andolina,[†] and Wissam A. Saidi*

Cite This: *J. Phys. Chem. Lett.* 2023, 14, 8741−8748

Read Online

ACCESS | Metrics & More | Article Recommendations | Supporting Information

ABSTRACT: While accurate measurements of MgO under extreme high-pressure conditions are needed to understand and model planetary behavior, these studies are challenging from both experimental and computational modeling perspectives. Herein, we accelerate density functional theory (DFT) accurate calculations using deep neural network potentials (DNPs) trained over multiple phases and study the melting behavior of MgO via the two-phase coexistence (TPC) approach at 0−300 GPa and ≤9600 K. The resulting DNP−TPC melting curve is in excellent agreement with existing experimental studies. We show that the mitigation of finite-size effects that typically skew the predicted melting temperatures in DFT−TPC simulations in excess of several hundred kelvin requires models with ∼16 000 atoms and >100 ps molecular dynamics trajectories. In addition, the DNP can successfully describe MgO metallization well at increased pressures that are captured by DFT but missed by classical interatomic potentials.

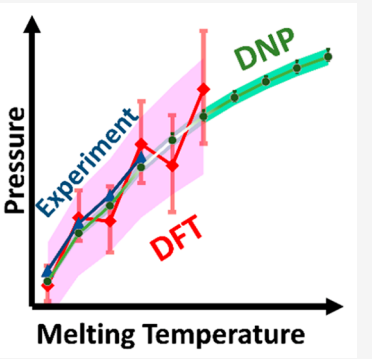

To discern the planetary behavior of Earth and other planets within and beyond the solar system, it is important to understand magnesium oxide (MgO), one of the most abundant components in the interiors of these heavenly bodies.[1−6] Of particular interest are the high-pressure and -temperature conditions that mimic the planetary interior and provide a fundamental understanding of geoscience and astrogeology.[7,8] Under Earth's mantle condition, MgO exists in a rock salt structure.[9,10] The melting temperatures of MgO under these extreme conditions are utilized to build accurate models related to the mineralogy of the Earth's crust and its relation to seismic activities.[7,11−13]

Few experimental studies have focused on the melting behavior of MgO.[14−17] Even though these studies investigated only a limited range of pressures compared to what exists in the interior of the Earth and other planets, the experimental results are not in full agreement. For instance, while the shock experiments explore temperatures of >5000 K and pressures of >300 GPa,[14] the resulting melting curve is inconsistent with the experimental results utilizing the more conventional laser-heated diamond anvil cell (DAC).[15] Similarly, melting curves gained from laser-heated DAC and resistance heating measurements yielded contrasting results.[16,17] The inconsistencies in these studies underscore the experimental challenges under extreme conditions, which is likely to be a general finding with other systems.

Computational modeling based on first-principles density functional theory (DFT) calculations is advantageous for understanding the behavior of materials under extreme temperature and pressure conditions. For instance, a recent study has examined the anharmonicity and phase diagram of MgO in the megabar pressure regime.[18] Also, the melting curves of MgO under relatively high pressures have been calculated in several studies.[8,18−26] However, analogous to the experimental case, there is significant variability in the computed melting temperatures, particularly at increased pressures,[22−25] underscoring the complexity of these studies. Mainly melting temperature calculations are "large" in two domains: the number of atoms in the simulation models and the number of time steps to be propagated along the molecular dynamics (MD) trajectory to determine the equilibrium configuration under given temperature and pressure conditions. Standard DFT calculations are computationally expensive and do not scale well in these "large" regimes. Other factors, such as the use of different computational frameworks, could also be a factor in the variability of the results. While methods based on classical atomistic force fields can, in principle, replicate DFT energies and forces at a fraction of its cost, such efforts are nontrivial and require significant tailoring and human consideration. Indeed, it is argued that free energy errors of 0.01 eV/atom may produce a corresponding error of 100 K in the melting temperature.[27] Importantly for MgO, a potential challenge for classical atomic force fields is the change in the electronic structure from insulating to metallic behavior at high pressures and temperatures.[28,29] Thus, not surprisingly, there is appreciable

Received: August 29, 2023
Accepted: September 20, 2023
Published: September 22, 2023

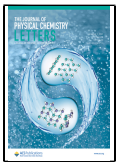

https://doi.org/10.1021/acs.jpclett.3c02424
J. Phys. Chem. Lett. 2023, 14, 8741−8748

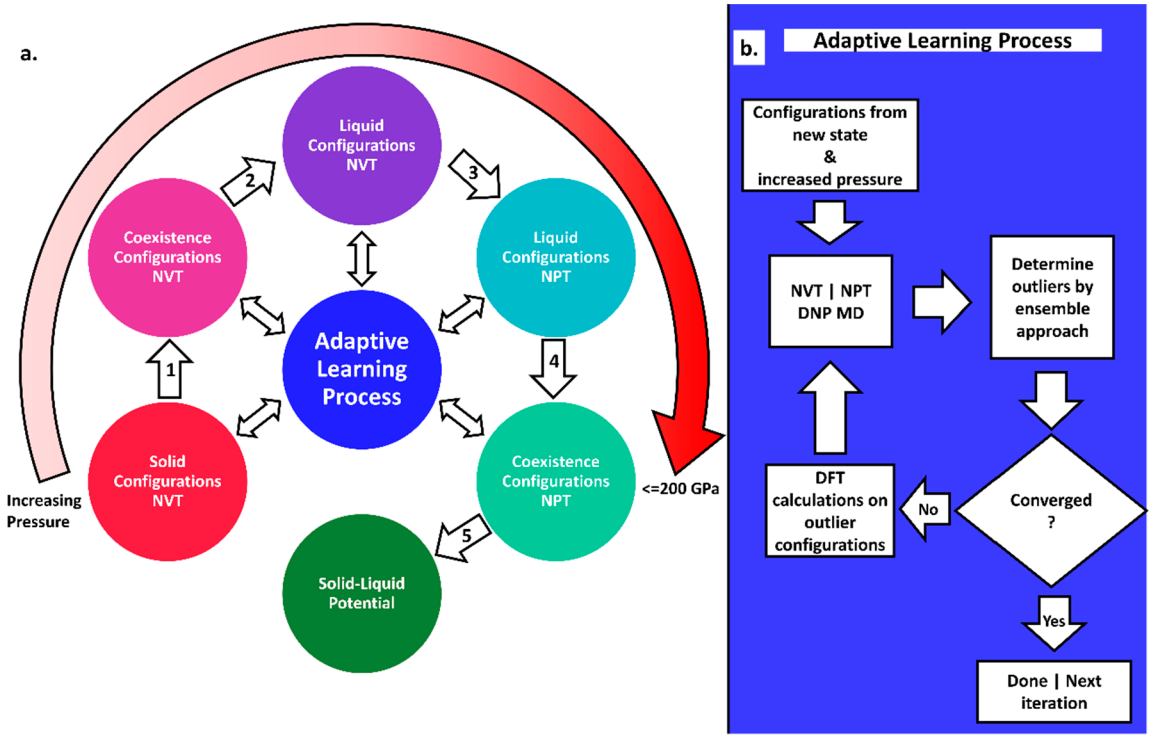

Figure 1. (a) Overall workflow in generating the data set for the DNP that encompasses the solid and liquid states of MgO at finite temperatures and pressures. (b) Adaptive-learning process employed in this study.

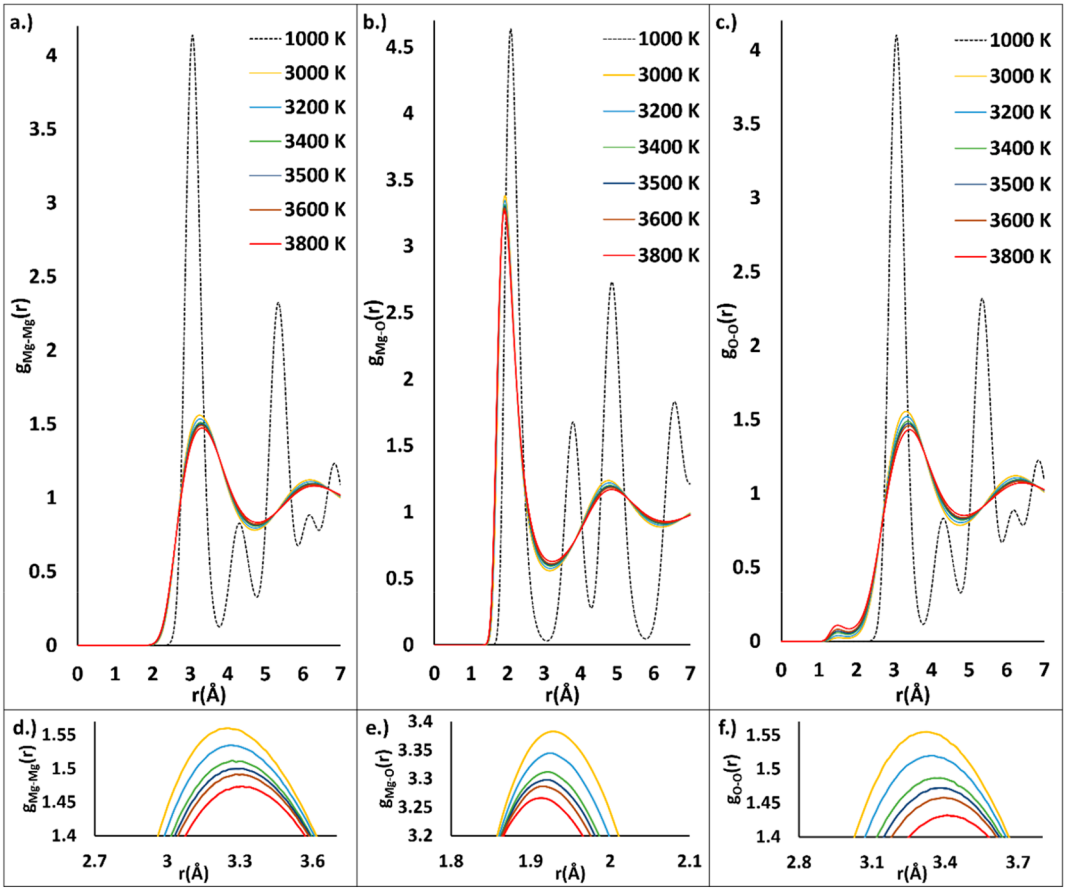

Figure 2. Partial radial distribution functions for (a and d) Mg−Mg, (b and e) Mg−O, and (c and f) O−O bonds. Panels d−e zoom in on the first peak of the liquid profiles. Panels a−c display the contrast of the profile between solid (1000 K) and liquid configurations.

https://doi.org/10.1021/acs.jpclett.3c02424
J. Phys. Chem. Lett. 2023, 14, 8741−8748

variability of the data reported using classical atomistic potentials, particularly at high pressures of >50 GPa[29−31] (see also Figure 4). Therefore, there is a need to develop robust and accurate atomistic potentials to enable large-scale simulations in both size and time domains beyond what can be done with first-principles methods.

Recent advancements in machine learning and deep learning have enabled rapid simulations of materials for different applications.[32−37] In particular, deep neural network potentials (DNPs) allowed for the development of transferable and efficient machine-learned interatomic potentials that have accuracy similar to that of DFT but are orders of magnitude computationally faster.[38−46] For example, it has been previously demonstrated that DNPs can reliably replicate DFT values across different systems, including elemental[47] and binary[48,49] metals, supported metal nanoclusters,[50] hybrid perovskites,[51] and metal oxides.[52] We posit that DNPs can also be successfully applied at extreme temperature and pressures spanning the different phases for MgO and can successfully describe the changes in electronic structure from insulating to metallic behavior as pressure increases to mantle conditions.

In our study, the MgO DNP was trained through an adaptive-learning loop building on the low-temperature and low-pressure database published previously.[52] Our recent study showed that DNPs can describe with high fidelity a variety of solid metal oxides, including MgO, each having different polymorphs and with different oxidation states for the metal.[52] Notably, the DNP described the thermal expansion of solid MgO well, yielding results in agreement with DFT and experimental results.[52] Extending the DNP in the melting regime and for high pressures requires augmenting the database, mainly in the liquid phase and at the solid−liquid interface (see Figure 1). However, compared to that in the solid phase, DNP validation in these disorderly phases is more complex because of the high likelihood of encountering a configuration with a low degree of similarity to any configuration in the training data set, especially at increased pressures and temperatures. Thus, it is anticipated that simulating the liquid and the solid−liquid interface with a high degree of fidelity requires a significant increase in data set size and pushes the extrapolation regime of the DNP. This systematic enhancement approach we took is depicted in Figure 1a. See Methodology for further details.

First, we applied the DNP on the liquid phase of MgO by computing at finite temperatures the partial radial distribution function (RDF), $g(r)$, which describes the likelihood of finding another atom within a distance r of a given atom.[53] See Methodology for details. Figure 2 shows the RDF at temperatures ranging from 1000 to 3800 K at zero pressure. These contrasting temperatures were intentionally set up to test and verify the capability of the DNP to correctly describe MgO under solid (e.g., T = 1000 K) and liquid conditions[19,29,31,54,55] (e.g., T = 3000 K), as any failure would be readily apparent. The sharp peaks of the RDF at 1000 K, as shown in Figure 2b, indicate a long-range order consistent with the solid phase. The first peak located at 2.08 Å is comparable, albeit not the same due to thermal effects, to the Mg−O nearest neighbor distance for solid MgO of 2.1 Å. At the highest temperatures of >3000 K, the RDFs in Figure 2a−c display a uniform broadening, indicating a liquid phase. These results point to the undiminished capability of the potential to model solid and liquid MgO phases, while validating our process of obtaining the partial RDF profile.

Thermal effects on the liquid phase can be closely scrutinized in Figure 2d−f, which shows a close look at the prominent peaks of Figure 2a−c. Namely, the increased broadening of the first peak with temperature reflects an increasing level of disorder in the systems; i.e., the peak becomes flatter at higher temperatures as the level of short-range order decreases. The broadening of the peaks is also due to the thermal expansion of the system, evidenced by the increase in the nearest neighbor distances; all of this was captured well by the potential. Karki et al.[20] reported a first peak at 3000 K to be at 1.963 Å using ab initio molecular dynamics, which compares well to the first peak in panels b and e of Figure 2 of 1.925 Å. The slight difference may be attributed to the different ensemble [constant volume and temperature (NVT)] employed in the previous study, while our study employs constant pressure and temperature (NPT), which does not restrict the liquid's changes in volume. This comparison demonstrates that the DNP captures the liquid MgO behavior like DFT does.

Thermal changes in the bond distances extracted from the MD trajectory are summarized in Table S1. We note that Mg−O, Mg−Mg, and O−O bonds are unbroken even at the highest temperature investigated, 3800 K, consistent with the stability of MgO observed in experimental studies.[54] Interestingly, as the temperature increased from 3000 to 3800 K, the average Mg−O bond was shortened by −0.72%, while the average bond between the same types of atoms we lengthened (1.72% and 2.53% for Mg−Mg and O−O, respectively). Similar observations are reported in the simulation of liquid NaCl.[56] Thus, we posit that the lengthening of average distances between like atoms is the main contributor to the thermal expansion of the system. In addition, the bond length can be correlated with binding free energy ΔF, which can be approximated from the pair distribution function for different species as $\Delta F = -k_b T \log[g_{Mg-O}(r)]$[57] for a given bond length r. The change in the Mg−O bond distance in Figure 2e reflects the strengthening of the bond's binding free energy from −0.14 eV at 3000 K to −0.17 eV at 3800 K. Also, in contrast with NaCl, the Na−Cl binding free energy becomes stronger by ∼10% as the temperature increases by 150 K,[56] while the Mg−O binding free energy is less strengthened with an increase in temperature.

To study MgO under melting conditions and determine the melting temperature, we utilized the two-phase coexistence (TPC) approach that stipulates the equality of the free energy of the solid and liquid phases at the melting temperature by employing a contiguous system containing both phases.[58,59] See Figure S2 for a visual description of the system and process. TPC is particularly well suited to MD techniques due to how total energies are conserved in conventional MD schemes. Namely, for temperatures outside the melting curve, the excess or lack of latent heat will melt or solidify, respectively, the entire system as it approaches equilibrium. In addition, the two phases interfacing with each other will mitigate issues that may originate from nucleation barriers of either phase.[59]

The practical application of TPC involves multiple factors that significantly increase the number of different calculations and their respective costs. First, the TPC approach, by design, utilizes a trial-and-error method to determine the melting curve: it commences with an "informed" guess of the temperature ($T_{m,guess}$), which is then increased or decreased in the subsequent iterations if the solid−liquid equilibrium is

https://doi.org/10.1021/acs.jpclett.3c02424
J. Phys. Chem. Lett. 2023, 14, 8741−8748

not achieved until a temperature is found that leads to the coexistence of the solid and liquid phases. Second, fluctuations in the system must be minimized to obtain accurate results. This can be readily appreciated given that temperature and pressure fluctuations in the *NPT* ensemble decrease slowly as $1/\sqrt{N}$ with the number of atoms (N) in the system. Furthermore, the atomic equations of motion within the molecular dynamics simulations must be propagated for a long time, approximately tens of picoseconds, ensuring the system has minimal fluctuations. Third, there is statistical uncertainty in the obtained melting temperature due to the stochastic nature of the TPC approach, instigated with random initialization of atomic velocities consistent with a given temperature. These uncertainties can be quantified using only an ensemble approach. In summary, these complications strongly motivate the use of an accurate atomistic approach, as enabled by DNP, instead of direct DFT calculations to obtain accurate melting temperatures.

The variations of the TPC results with the model setup are examined first to assess the finite-size effects in the space and time domains. Figure 3a shows the change in the kinetic energy for four different model sizes ranging from 3 × 3 × 6 (432 atoms) to 20 × 20 × 40 (128 000 atoms) as a function of the total propagation time with each at zero pressure. We use the change in the kinetic energy or atom to determine when the TPC has reached equilibrium, as indicated by its convergence as a function of simulation time. We also visually inspect simulation trajectories to ensure the two phases are present, which could be achieved using RDFs, densities, or polyhedral template matching approaches. As shown in the figure, for the smallest system size of 432 atoms, we observe large thermal fluctuations that inhibit the establishment of the two phases; hence, smaller system sizes require more simulation time to equilibrate the liquid and solid phases. In contrast, the larger supercells reached convergence within the simulation time, as shown in the figure.

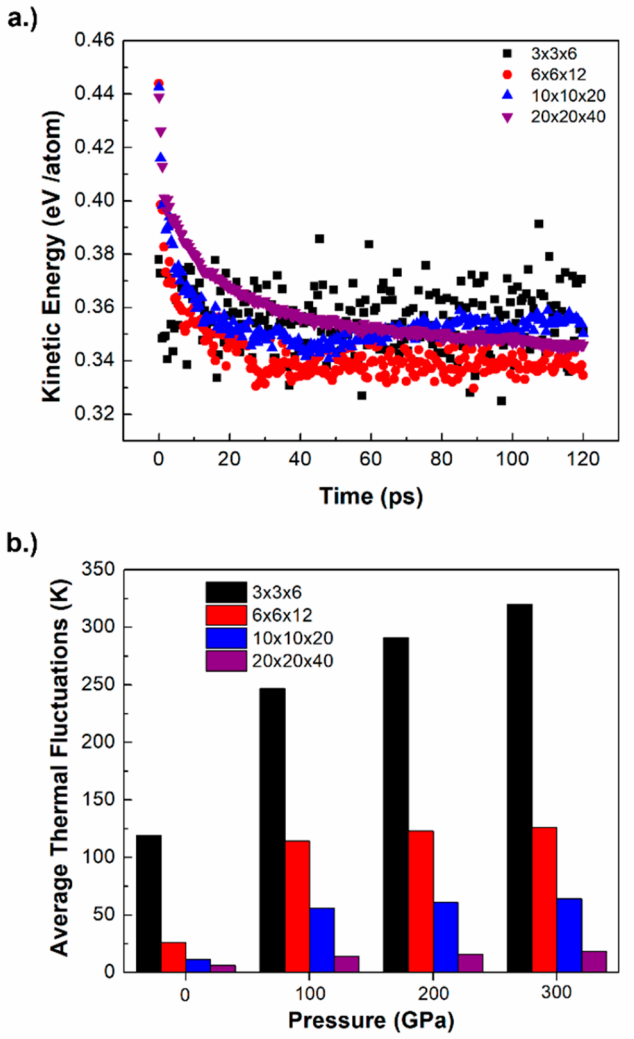

Figure 3. (a) Changes in the kinetic energy per atom during thermal equilibration of the TPC simulation for different system sizes at 0 GPa. (b) Average thermal fluctuations for different system sizes at different pressures.

Simulations at finite pressures also increase the fluctuations in the system compared to that at ambient pressure. We tested the four supercells with pressures of ≤300 GPa to elucidate this behavior, as shown in Figure 3b. The smallest supercell size, 3 × 3 × 6, exhibits a significant deviation in temperature, especially at increased pressures. We note that the thermal fluctuations of ∼120 K for individual simulations were too large to have a stable TPC with a 3 × 3 × 6 supercell (432 atoms!). At 0 GPa, the fluctuations are reduced by less than half, ∼25 K for a 6 × 6 × 12 supercell, an order of magnitude ∼12 K for a 10 × 10 × 20 supercell, and ∼5 K for the 20 × 20 × 40 supercell. Overall, it is clear that an increasing pressure (temperature) correlates to increasing fluctuations in the system. The thermal fluctuations increase ∼2.5 times as the pressure increases from 0 to 300 GPa. Thus, high-pressure TPC simulations necessitate larger supercells as opposed to lower pressures to mitigate these fluctuations.

Following guidance on the appropriate simulation parameters obtained from the aforementioned convergence tests, we performed production calculations using a 10 × 10 × 20 supercell with 16 000 atoms for pressures ranging from 0 to 300 GPa. The MD equations of motion are propagated for 120 ps, where we used the first 100 ps for the TPC to reach equilibrium and the last 20 ps to generate the melting temperature and standard deviation. In addition, we assess the statistical significance of the results by carrying out five TPC simulations with different initial velocities and using the ensemble approach to compute the mean and standard deviation of the melting temperature. Figure 4 depicts the melting behavior obtained from our simulations and previous studies. As shown in the figure, the overall trend shows an increase in the melting temperature with pressure, consistent with other rock salt systems such as NaCl[61] and LiH,[62] albeit these compounds melt at appreciably lower temperatures.

The comparison of our results to those obtained from classical interatomic potentials shows mixed results, as depicted in Figure 4. At lower pressures of <50 GPa, the DNP results generally match well with those of Belonoshko et al. using an interatomic potential based on empirical results for MgO-SiO_2[55] and Belonoshko et al. with the Matsui model.[29,63] In contrast, we did not find agreement with Strachan et al.,[60] likely because their classical force field[31] was trained on only the solid phase. For high pressures of >50 GPa, we have less agreement likely because classical interatomic potentials cannot capture well both the insulating behavior at low pressures and the metallic one of liquid MgO at high pressures (>50 GPa).[28,29] DFT and, by extension, DNP can capture such changes well. Hence, the slopes of the two former studies with

https://doi.org/10.1021/acs.jpclett.3c02424
J. Phys. Chem. Lett. 2023, 14, 8741−8748

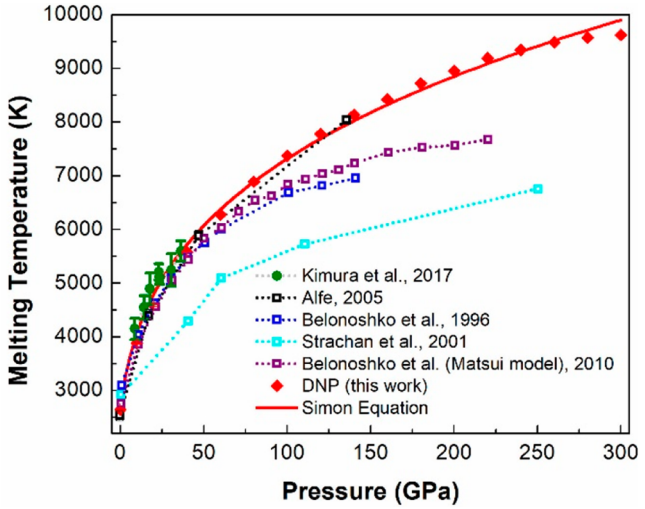

Figure 4. Melting curves for MgO from this work compared with that from an experimental study by Kimura et al.,[15] DFT results from Alfé,[19] the Matsui model from Belonoshko et al.,[29] and classical potentials from Strachan et al.[60] and Belonoshko et al.[55] Statistical uncertainties in the DNP results are represented as the error of five TPC simulations with different random seeds. They are smaller than the symbols and are not visible in the plot. The DNP equation matches well what is expected from the Simon equation.

classical potentials are found to diverge from our results at high pressures.

In addition, Figure 4 shows good agreement between the DNP and the DFT results with the PBE exchange-correlation functional performed by Alfé[19] using a similar TPC approach. At zero pressure, the melting temperature from Alfé of ∼2530 K appreciably underestimates our value of 2644 K, as well as that of another recent DFT[64] study, ∼2750 K,[64] obtained from the free energy method that used the same exchange-correlation functional. These underestimations may be due to the finite-size effect, as discussed above, or the use of the *NVT* ensemble in the DFT simulations rather than the more computationally demanding but more accurate *NPT* ensemble. We note that the DFT values at zero pressure all underestimate the experimental results of 3098 ± 42 K from Kimura et al.[15] and ∼3050 K[65] from Zerr and Boehler. We posit that this discrepancy is due to intrinsic errors in the employed exchange-correlation functional (PBE) that generally underestimates the melting temperature.[66,67]

Figure 4 also shows the experimental results of Kimura et al.,[15] who determined MgO melting at finite pressures through laser-heated DAC at pressures of ≲50 GPa. As shown in the figure, the DNP results are in excellent agreement with the experimental results in this relatively low-pressure range. To gain more insight, we also employ the Simon model[68] $T_m = T_0\left(\frac{P_m}{A} + 1\right)^{1/C}$ that empirically describes the increase in melting temperature T_m as a function of pressure P_m. Here, T_0 is the melting temperature at zero pressure, and A and C are empirical constants. From the fit using pressures of ≲50 GPa, the A and C values are 12.0 and 2.5, respectively, which compare well to the corresponding experimental values[15] of 11.1 ± 4.0 and 2.7 ± 0.5, respectively. Using the complete melting data at pressures of ≲300 GPa, we found good agreement with the Simon model (Figure 4, red line) with an R^2 fit of 0.99. The respective A and C values of 5.9 and 3.4 are appreciably different than the corresponding values obtained in the lower-pressure regime, which is not surprising owing to the change in the curvature of the melting curve at higher temperatures and pressures.

In conclusion, we have performed large-scale simulations at increased pressures and temperatures for MgO's solid, liquid, and liquid−solid systems. While MgO can be considered a simple system, creating a melting curve and observing its liquid properties add significant complexities, given the high melting temperature. Despite DFT being able to perform these simulations, we have observed that at the scale even with ∼1000-atom models, there are significant fluctuations in the system exacerbated by high pressures that affect the accuracy of the results. Conversely, trends such as the changing nature of the material electronic structure from insulating to metallic with an increase in pressure, which DFT readily captures, may be missed by classical interatomic potentials typically used as a supplement or substitute to surpass DFT-scale limitations. Hence, the rapid development of potentials that can overcome the computational cost barriers while staying DFT-accurate, such as DNPs, would be essential to such studies. In addition, such a cost reduction can also be leveraged to investigate factors such as finite-size effects and to quantify statistical uncertainties. Finally, this study demonstrated that an existing DNP database could be utilized as a launchpad to rapidly generate a DNP specialized for a detailed study involving multiple phases and yield results comparable to those of DFTs. As the generation of melting curves at high temperatures and pressures is explored for other materials, such approaches that can save real and computational time in both the potential preparation and simulation itself would allow acceleration of the development of the field.

METHODOLOGY

The DNP was developed with the DeepPot-SE method[69] as implemented in DeePMD-Kit.[40] The adaptive-learning process that we employed is shown in Figure 1b. We initialized the DNP with the data set from our previous work[52] that has 13 390 configurations based on experimentally verified MgO structures cubic MgO_2, rock salt MgO, and $P6_3mc$ and $P\bar{6}m2$ hexagonal MgO. We augment the data set through an iterative-learning process focusing on the liquid and solid−liquid coexistence regimes not investigated in the old data set. We followed the melting curve generated through two-phase coexistence by Alfé.[19] At each point of interest in the melting curve, we ran the ensemble of five potentials and chose configurations with force deviations between 0.2 and 1.0 eV/Å to be calculated with DFT and added to the data set. Consistent with the original data set, the additional configurations were calculated with Vienna *Ab initio* Simulation Package (VASP)[70−72] using the same computational framework, i.e., the *NVT* (constant volume and temperature) ensemble at a 2 fs time step for 20 steps (more details can be found in our previous work).[52] The resulting data set employed in the study presented here was achieved after 13 iterations, adding 31 402 configurations, leading to the data set having a total of 44 792. The additional configurations of liquid and solid−liquid phases consist of 27 643 configurations from a 2 × 2 × 2 supercell (64 atoms) and 3759 configurations from a 2 × 2 × 4 supercell (128 atoms). Considering the lack of long-range order in the targeted phases at high temperatures and pressures, we found a significant increase in the number of configurations to be reasonable. In-depth discussion of the

https://doi.org/10.1021/acs.jpclett.3c02424
J. Phys. Chem. Lett. 2023, 14, 8741−8748

DFT calculation parameters, DNP generation, and how the potential performed for solid MgO can be found in our previous work.[52] The atomistic calculations were carried out using LAMMPS.[73]

Liquid Phase and RDF Generation. To obtain the partial RDF, the liquid phase is generated by employing molecular dynamics (MD) simulation with the Langevin thermostat[74] with a microcanonical ensemble (*NVE*) at a targeted temperature for 50 ps with a 2 fs time step. This is followed by equilibration with the canonical ensemble (*NVT*) for 100 ps to ensure stability. The production run utilized the NPT ensemble (constant pressure and temperature) at the targeted temperature and pressure for 2 ns, from which we calculate the partial RDF profile at increasing temperatures in a 5 × 5 × 5 supercell (1000 atoms).

Accounting for the stochastic nature of the DNP, which is determined with a stochastic optimization approach that is highly likely to converge to different local minima, we performed all calculations with an ensemble of five different potentials obtained from different random seeds. All reported values are averages from the ensemble. For instance, for the RDFs, the maximum deviation for the Mg−O partial RDF is 0.027 at 3800 K while the corresponding deviations for Mg−Mg and O−O are an order of magnitude smaller. We can surmise that the potential ensemble is stable and consistent for liquid configurations.

Two-Phase Coexistence Simulation. TPC simulations first minimize the entire supercell at the target pressure. The entire supercell is next heated at the melting temperature "informed guess" $T_{m,guess}$ for 10 ps using a 2 fs time step and the *NPT* ensemble at a given finite pressure. The simulation box is partitioned along the *z*-axis along MgO (001), with the bottom half treated as the liquid section and the upper half treated as the solid section. The liquid section is heated by increasing the temperature to ∼1.3 times the $T_{m,guess}$ to ensure complete melting for a 5 ps duration, followed by cooling to ∼1.1 times the $T_{m,guess}$ for 10 ps. These temperature ranges were adjusted for different supercells and pressures. Finally, the isenthalpic ensemble (*NPH*) is applied to the entire simulation box at a given pressure of 120 ps using a 1 fs time step to allow for temperature and pressure equilibration. The last 20 ps of the equilibration was used to determine the mean T_m and pressure and the associated standard deviation. To estimate the simulation-to-simulation variation, we changed the seed number to generate the initial atomistic velocities in the heating step and determined the mean T_m and pressure and the associated deviation for five randomly seeded simulations.

■ ASSOCIATED CONTENT

Supporting Information

The Supporting Information is available free of charge at https://pubs.acs.org/doi/10.1021/acs.jpclett.3c02424.

A table listing first RDF peaks, a table listing DNP melting curve data points, a figure and an analysis of the partial RDF with respect to system size, a figure visualizing the TPC simulation, a figure of thermal fluctuation as a function of system size, and a table showing thermal fluctuations for a 10 × 10 × 20 supercell from 0 to 300 GPa (PDF)

■ AUTHOR INFORMATION

Corresponding Author

Wissam A. Saidi − *Department of Mechanical Engineering and Materials Science, University of Pittsburgh, Pittsburgh, Pennsylvania 15216, United States;* orcid.org/0000-0001-6714-4832; Email: alsaidi@pitt.edu

Authors

Pandu Wisesa − *Department of Mechanical Engineering and Materials Science, University of Pittsburgh, Pittsburgh, Pennsylvania 15216, United States;* orcid.org/0000-0001-8494-070X

Christopher M. Andolina − *Department of Mechanical Engineering and Materials Science, University of Pittsburgh, Pittsburgh, Pennsylvania 15216, United States;* orcid.org/0000-0003-2157-9114

Complete contact information is available at: https://pubs.acs.org/10.1021/acs.jpclett.3c02424

Author Contributions

†P.W. and C.M.A. contributed equally to this work.

Notes

The authors declare no competing financial interest.

The compiled potential and training data set can be found on GitHub (https://github.com/saidigroup/Metal-Oxide-Dataset) or at DOI 10.5281/zenodo.8368724.

■ ACKNOWLEDGMENTS

The authors are grateful to the U.S. National Science Foundation (NSF) (Grant CSSI-2003808). This research was supported in part by the University of Pittsburgh Center for Research Computing through the resources provided. Specifically, this work used the H2P cluster, which is supported by NSF Grant OAC-2117681.

■ REFERENCES

(1) Ringwood, A. E. Phase Transformations and Their Bearing on the Constitution and Dynamics of the Mantle. *Geochim. Cosmochim. Acta* **1991**, *55* (8), 2083−2110.

(2) Shand, M. A. *The Chemistry and Technology of Magnesia*; Wiley-Interscience: Hoboken, NJ, 2006.

(3) Valencia, D.; O'Connell, R. J.; Sasselov, D. Internal Structure of Massive Terrestrial Planets. *Icarus* **2006**, *181* (2), 545−554.

(4) Stixrude, L. Melting in Super-Earths. *Philosophical Transactions of the Royal Society A: Mathematical, Physical and Engineering Sciences* **2014**, *372* (2014), 20130076.

(5) Nettelmann, N.; Helled, R.; Fortney, J. J.; Redmer, R. New Indication for a Dichotomy in the Interior Structure of Uranus and Neptune from the Application of Modified Shape and Rotation Data. *Planetary and Space Science* **2013**, *77*, 143−151.

(6) Nettelmann, N.; Wang, K.; Fortney, J. J.; Hamel, S.; Yellamilli, S.; Bethkenhagen, M.; Redmer, R. Uranus Evolution Models with Simple Thermal Boundary Layers. *Icarus* **2016**, *275*, 107−116.

(7) Lay, T.; Williams, Q.; Garnero, E. J. The Core-Mantle Boundary Layer and Deep Earth Dynamics. *Nature* **1998**, *392* (6675), 461−468.

(8) Gillan, M. J.; Alfè, D.; Brodholt, J.; Vočadlo, L.; Price, G. D. First-Principles Modelling of Earth and Planetary Materials at High Pressures and Temperatures. *Rep. Prog. Phys.* **2006**, *69* (8), 2365−2441.

(9) Svendsen, B.; Ahrens, T. J. Shock-Induced Temperatures of MgO. *GeoJI* **1987**, *91* (3), 667−691.

(10) Duffy, T. S.; Hemley, R. J.; Mao, H.-k. Equation of State and Shear Strength at Multimegabar Pressures: Magnesium Oxide to 227 GPa. *Phys. Rev. Lett.* **1995**, *74* (8), 1371−1374.

(11) Dziewonski, A. M.; Anderson, D. L. Preliminary Reference Earth Model. *PEPI* **1981**, *25* (4), 297−356.
(12) Matzel, E.; Sen, M. K.; Grand, S. P. Evidence for Anisotropy in the Deep Mantle beneath Alaska. *Geophys. Res. Lett.* **1996**, *23* (18), 2417−2420.
(13) Garnero, E. J.; Lay, T. Lateral Variations in Lowermost Mantle Shear Wave Anisotropy beneath the North Pacific and Alaska. *Journal of Geophysical Research: Solid Earth* **1997**, *102* (B4), 8121−8135.
(14) McWilliams, R. S.; Spaulding, D. K.; Eggert, J. H.; Celliers, P. M.; Hicks, D. G.; Smith, R. F.; Collins, G. W.; Jeanloz, R. Phase Transformations and Metallization of Magnesium Oxide at High Pressure and Temperature. *Science* **2012**, *338* (6112), 1330−1333.
(15) Kimura, T.; Ohfuji, H.; Nishi, M.; Irifune, T. Melting Temperatures of MgO under High Pressure by Micro-Texture Analysis. *Nat. Commun.* **2017**, *8* (1), 15735.
(16) Zhang, L.; Fei, Y. Melting Behavior of (Mg, Fe)O Solid Solutions at High Pressure. *Geophys. Res. Lett.* **2008**, *35* (13), n/a.
(17) Du, Z.; Lee, K. K. M. High-Pressure Melting of MgO from (Mg, Fe)O Solid Solutions. *Geophys. Res. Lett.* **2014**, *41* (22), 8061−8066.
(18) Soubiran, F.; Militzer, B. Anharmonicity and Phase Diagram of Magnesium Oxide in the Megabar Regime. *Phys. Rev. Lett.* **2020**, *125* (17), 175701.
(19) Alfè, D. Melting Curve of MgO from First-Principles Simulations. *Phys. Rev. Lett.* **2005**, *94* (23), 235701.
(20) Karki, B. B.; Bhattarai, D.; Stixrude, L. First-Principles Calculations of the Structural, Dynamical, and Electronic Properties of Liquid MgO. *Phys. Rev. B* **2006**, *73* (17), 174208.
(21) Karki, B. B.; Wentzcovitch, R. M.; de Gironcoli, S.; Baroni, S. First-Principles Determination of Elastic Anisotropy and Wave Velocities of MgO at Lower Mantle Conditions. *Science* **1999**, *286* (5445), 1705−1707.
(22) Boates, B.; Bonev, S. A. Demixing Instability in Dense Molten MgSiO and the Phase Diagram of MgO. *Phys. Rev. Lett.* **2013**, *110* (13), 135504.
(23) Root, S.; Shulenburger, L.; Lemke, R. W.; Dolan, D. H.; Mattsson, T. R.; Desjarlais, M. P. Shock Response and Phase Transitions of MgO at Planetary Impact Conditions. *Phys. Rev. Lett.* **2015**, *115* (19), 198501.
(24) Miyanishi, K.; Tange, Y.; Ozaki, N.; Kimura, T.; Sano, T.; Sakawa, Y.; Tsuchiya, T.; Kodama, R. Laser-Shock Compression of Magnesium Oxide in the Warm-Dense-Matter Regime. *Phys. Rev. E* **2015**, *92* (2), 023103.
(25) Taniuchi, T.; Tsuchiya, T. The Melting Points of MgO up to 4 Tpa Predicted Based on Ab Initio Thermodynamic Integration Molecular Dynamics. *J. Phys.: Condens. Matter* **2018**, *30* (11), 114003.
(26) Cebulla, D.; Redmer, R. Ab Initio Simulations of MgO under Extreme Conditions. *Phys. Rev. B* **2014**, *89* (13), 134107.
(27) Foiles, S. M.; Adams, J. B. Thermodynamic Properties of fcc Transition Metals as Calculated with the Embedded-Atom Method. *Phys. Rev. B* **1989**, *40* (9), 5909−5915.
(28) Drummond, N. D.; Ackland, G. J. Ab Initio Quasiharmonic Equations of State for Dynamically Stabilized Soft-Mode Materials. *Phys. Rev. B* **2002**, *65* (18), 184104.
(29) Belonoshko, A. B.; Arapan, S.; Martonak, R.; Rosengren, A. MgO Phase Diagram from First Principles in a Wide Pressure-Temperature Range. *Phys. Rev. B* **2010**, *81* (5), 054110.
(30) Belonoshko, A. B. Molecular Dynamics of MgSiO3 Perovskite at High Pressures: Equation of State, Structure, and Melting Transition. *Geochim. Cosmochim. Acta* **1994**, *58* (19), 4039−4047.
(31) Strachan, A.; Çağin, T.; Goddard, W. A. Phase Diagram of MgO from Density-Functional Theory and Molecular-Dynamics Simulations. *Phys. Rev. B* **1999**, *60* (22), 15084−15093.
(32) Saidi, W. A. Emergence of Local Scaling Relations in Adsorption Energies on High-Entropy Alloys. *npj Comput. Mater.* **2022**, *8* (1), 86.
(33) Saidi, W. A.; Shadid, W.; Veser, G. Optimization of High-Entropy Alloy Catalyst for Ammonia Decomposition and Ammonia Synthesis. *J. Phys. Chem. Lett.* **2021**, *12* (21), 5185−5192.
(34) Saidi, W. A. Optimizing the Catalytic Activity of Pd-Based Multinary Alloys toward Oxygen Reduction Reaction. *J. Phys. Chem. Lett.* **2022**, *13* (4), 1042−1048.
(35) Zhou, Y.; Ouyang, Y.; Zhang, Y.; Li, Q.; Wang, J. Machine Learning Assisted Simulations of Electrochemical Interfaces: Recent Progress and Challenges. *J. Phys. Chem. Lett.* **2023**, *14* (9), 2308−2316.
(36) Naseri, M.; Gusarov, S.; Salahub, D. R. Quantum Machine Learning in Materials Prediction: A Case Study on Abo3 Perovskite Structures. *J. Phys. Chem. Lett.* **2023**, *14* (31), 6940−6947.
(37) Aditya, A.; Mishra, A.; Baradwaj, N.; Nomura, K.-i.; Nakano, A.; Vashishta, P.; Kalia, R. K. Wrinkles, Ridges, Miura-Ori, and Moiré Patterns in Mose2 Using Neural Networks. *J. Phys. Chem. Lett.* **2023**, *14* (7), 1732−1739.
(38) Bartók, A. P.; Payne, M. C.; Kondor, R.; Csányi, G. Gaussian Approximation Potentials: The Accuracy of Quantum Mechanics, without the Electrons. *Phys. Rev. Lett.* **2010**, *104* (13), 136403.
(39) Shapeev, A. V. Moment Tensor Potentials: A Class of Systematically Improvable Interatomic Potentials. *Multiscale Model. Simul.* **2016**, *14* (3), 1153−1173.
(40) Wang, H.; Zhang, L.; Han, J.; E, W. Deepmd-Kit: A Deep Learning Package for Many-Body Potential Energy Representation and Molecular Dynamics. *Comput. Phys. Commun.* **2018**, *228*, 178−184.
(41) Lee, K.; Yoo, D.; Jeong, W.; Han, S. Simple-Nn: An Efficient Package for Training and Executing Neural-Network Interatomic Potentials. *Comput. Phys. Commun.* **2019**, *242*, 95−103.
(42) Sivaraman, G.; Gallington, L.; Krishnamoorthy, A. N.; Stan, M.; Csányi, G.; Vázquez-Mayagoitia, Á.; Benmore, C. J. Experimentally Driven Automated Machine-Learned Interatomic Potential for a Refractory Oxide. *Phys. Rev. Lett.* **2021**, *126* (15), 156002.
(43) Kocer, E.; Ko, T. W.; Behler, J. Neural Network Potentials: A Concise Overview of Methods. *Annu. Rev. Phys. Chem.* **2022**, *73* (1), 163−186.
(44) Kulichenko, M.; Smith, J. S.; Nebgen, B.; Li, Y. W.; Fedik, N.; Boldyrev, A. I.; Lubbers, N.; Barros, K.; Tretiak, S. The Rise of Neural Networks for Materials and Chemical Dynamics. *J. Phys. Chem. Lett.* **2021**, *12* (26), 6227−6243.
(45) Behler, J.; Parrinello, M. Generalized Neural-Network Representation of High-Dimensional Potential-Energy Surfaces. *Phys. Rev. Lett.* **2007**, *98* (14), 146401.
(46) Krenzer, G.; Klarbring, J.; Tolborg, K.; Rossignol, H.; McCluskey, A. R.; Morgan, B. J.; Walsh, A. Nature of the Superionic Phase Transition of Lithium Nitride from Machine Learning Force Fields. *Chem. Mater.* **2023**, *35* (15), 6133−6140.
(47) Bayerl, D.; Andolina, C. M.; Dwaraknath, S.; Saidi, W. A. Convergence Acceleration in Machine Learning Potentials for Atomistic Simulations. *Digital Discovery* **2022**, *1* (1), 61−69.
(48) Andolina, C. M.; Wright, J. G.; Das, N.; Saidi, W. A. Improved Al-Mg Alloy Surface Segregation Predictions with a Machine Learning Atomistic Potential. *Phys. Rev. Mater.* **2021**, *5* (8), 083804.
(49) Andolina, C. M.; Williamson, P.; Saidi, W. A. Optimization and Validation of a Deep Learning Cuzr Atomistic Potential: Robust Applications for Crystalline and Amorphous Phases with near-Dft Accuracy. *J. Chem. Phys.* **2020**, *152* (15), 154701.
(50) Chu, W.; Saidi, W. A.; Prezhdo, O. V. Long-Lived Hot Electron in a Metallic Particle for Plasmonics and Catalysis: Ab Initio Nonadiabatic Molecular Dynamics with Machine Learning. *ACS Nano* **2020**, *14* (8), 10608−10615.
(51) Wang, B.; Chu, W.; Wu, Y.; Casanova, D.; Saidi, W. A.; Prezhdo, O. V. Electron-Volt Fluctuation of Defect Levels in Metal Halide Perovskites on a 100 Ps Time Scale. *J. Phys. Chem. Lett.* **2022**, *13* (25), 5946−5952.
(52) Wisesa, P.; Andolina, C. M.; Saidi, W. A. Development and Validation of Versatile Deep Atomistic Potentials for Metal Oxides. *J. Phys. Chem. Lett.* **2023**, *14*, 468−475.
(53) Allen, M. P.; Tildesley, D. J.; Allen, M. P.; Tildesley, D. J. How to Analyse the Results. In *Computer Simulation of Liquids*; Oxford University Press, 2017.

https://doi.org/10.1021/acs.jpclett.3c02424
J. Phys. Chem. Lett. 2023, 14, 8741−8748

(54) Haynes, W. M.; Lide, D. R.; Bruno, T. J. *CRC Handbook of Chemistry and Physics*, 97th ed.; CRC Press: Boca Raton, FL, 2017; Vol. *2016−2017*.
(55) Belonoshko, A. B.; Dubrovinsky, L. S. Molecular and Lattice Dynamics Study of the MgO-SiO2 System Using a Transferable Interatomic Potential. *Geochim. Cosmochim. Acta* **1996**, *60* (10), 1645−1656.
(56) Tovey, S.; Narayanan Krishnamoorthy, A.; Sivaraman, G.; Guo, J.; Benmore, C.; Heuer, A.; Holm, C. Dft Accurate Interatomic Potential for Molten NaCl from Machine Learning. *J. Phys. Chem. C* **2020**, *124* (47), 25760−25768.
(57) Smiatek, J.; Wohlfarth, A.; Holm, C. The Solvation and Ion Condensation Properties for Sulfonated Polyelectrolytes in Different Solvents—a Computational Study. *NJPh* **2014**, *16* (2), 025001.
(58) Vu, T. B.; García, N.; Dransfeld, K. *Nanosources and Manipulation of Atoms under High Fields and Temperatures: Applications*; Kluwer Academic Publishers: Dordrecht, The Netherlands, 1993.
(59) Morris, J. R.; Wang, C. Z.; Ho, K. M.; Chan, C. T. Melting Line of Aluminum from Simulations of Coexisting Phases. *Phys. Rev. B* **1994**, *49* (5), 3109−3115.
(60) Strachan, A.; Çağın, T.; Goddard, W. A. Reply tò Comment on ̀Phase Diagram of MgO from Density-Functional Theory and Molecular- Dynamics Simulations' ". *Phys. Rev. B* **2001**, *63* (9), 096102.
(61) Belonoshko, A. B.; Dubrovinsky, L. S. Molecular Dynamics of Nacl (B1 and B2) and MgO (B1) Melting: Two-Phase Simulation. *Am. Mineral.* **1996**, *81* (3−4), 303−316.
(62) Ogitsu, T.; Schwegler, E.; Gygi, F.; Galli, G. Melting of Lithium Hydride under Pressure. *Phys. Rev. Lett.* **2003**, *91* (17), 175502.
(63) Matsui, M. Molecular Dynamics Study of the Structural and Thermodynamic Properties of MgO Crystal with Quantum Correction. *J. Chem. Phys.* **1989**, *91* (1), 489−494.
(64) Rang, M.; Kresse, G. First-Principles Study of the Melting Temperature of MgO. *Phys. Rev. B* **2019**, *99* (18), 184103.
(65) Zerr, A.; Boehler, R. Constraints on the Melting Temperature of the Lower Mantle from High-Pressure Experiments on Mgo and Magnesioüstite. *Nature* **1994**, *371* (6497), 506−508.
(66) Zhang, G.-X.; Reilly, A. M.; Tkatchenko, A.; Scheffler, M. Performance of Various Density-Functional Approximations for Cohesive Properties of 64 Bulk Solids. *NJPh* **2018**, *20* (6), 063020.
(67) Hong, Q.-J. Melting Temperature Prediction Via First Principles and Deep Learning. *Comput. Mater. Sci.* **2022**, *214*, 111684.
(68) Simon, F.; Glatzel, G. Bemerkungen Zur Schmelzdruckkurve. *Zeitschrift für anorganische und allgemeine Chemie* **1929**, *178* (1), 309−316.
(69) Zhang, L.; Han, J.; Wang, H.; Saidi, W.; Car, R.; Weinan, E. End-to-End Symmetry Preserving Inter-Atomic Potential Energy Model for Finite and Extended Systems. *Advances in Neural Information Processing Systems 31 (NeurIPS 2018)*; 2018.
(70) Kresse, G.; Furthmüller, J. Efficient Iterative Schemes for Ab Initio Total-Energy Calculations Using a Plane-Wave Basis Set. *Phys. Rev. B* **1996**, *54* (16), 11169−11186.
(71) Shishkin, M.; Marsman, M.; Kresse, G. Accurate Quasiparticle Spectra from Self-Consistent Gw Calculations with Vertex Corrections. *Phys. Rev. Lett.* **2007**, *99* (24), 246403.
(72) Blöchl, P. E. Projector Augmented-Wave Method. *Phys. Rev. B* **1994**, *50* (24), 17953−17979.
(73) Thompson, A. P.; Aktulga, H. M.; Berger, R.; Bolintineanu, D. S.; Brown, W. M.; Crozier, P. S.; in 't Veld, P. J.; Kohlmeyer, A.; Moore, S. G.; Nguyen, T. D.; Shan, R.; Stevens, M. J.; Tranchida, J.; Trott, C.; Plimpton, S. J. Lammps - a Flexible Simulation Tool for Particle-Based Materials Modeling at the Atomic, Meso, and Continuum Scales. *Comput. Phys. Commun.* **2022**, *271*, 108171.
(74) Schneider, T.; Stoll, E. Molecular-Dynamics Study of a Three-Dimensional One-Component Model for Distortive Phase Transitions. *Phys. Rev. B* **1978**, *17* (3), 1302−1322.

https://doi.org/10.1021/acs.jpclett.3c02424
J. Phys. Chem. Lett. 2023, 14, 8741−8748